



Testing new CMOS pixel sensors for particle detection experiments with simulations

Larissa Mendes, DESY Summer Student Programme
Supervisors: Adriana Simancas and Anastasiia Velyka

8 September 2021

Abstract

Monolithic active pixel sensors manufactured in commercial CMOS technologies have been used in High Energy Physics (HEP) because of the many advantages in particle detection. In comparison to hybrid pixel technology, these devices integrate sensors and readout on a single chip with less material budget and manufacturing effort [5].

A new CMOS sensor technology is being investigated at DESY, for beam telescopes and vertex detectors in HEP experiments. Device simulations (TCAD) are required to understand the performance parameters of this technology.

Contents

1	Introduction	3
1.1	Charged Particles in Matter	3
1.2	Charge transport	4
1.3	Pixel detectors for lepton colliders	5
1.3.1	Monolithic detectors	5
1.4	EUDET Telescope	6
2	TCAD Simulations of the Monolithic Sensors	7
2.1	Model Details	8
2.2	Simulation Workspace	10
3	Simulation Results	10
3.1	Increasing p-well and backside voltage	10
3.2	Increasing backside voltage	12
3.3	Changing p-well opening	14
3.4	Conclusions	16

1 Introduction

Charged particle tracking and timing are fundamental tools for both physics research and for numerous applications. Although a number of detection techniques are available, silicon detectors have become largely employed due to their versatility and to the parallel strong developments of the semiconductor industry. Various flavours of silicon sensors have been developed to meet the specific requirements of different experiments and applications, such as high spatial resolution, fast charge collection, low power consumption, high radiation tolerance and low cost per unit area

1.1 Charged Particles in Matter

In the case of a charged particle with a mass above the electron mass ($M \gg m_e$) penetrating the material, ionization is the main process of energy loss. The Bethe-Bloch formula describes the average energy loss per distance.

$$-\left\langle \frac{dE}{dx} \right\rangle = 2\pi N_A r_e^2 m_e c^2 \rho \frac{Z}{A} \frac{z^2}{\beta^2} \left\{ \ln \left(\frac{2m_e c^2 \beta^2 \gamma^2 W_{max}}{I^2} \right) - 2\beta^2 - \delta(\beta\gamma) - \frac{C}{Z} \right\}$$

where r_e is the electron radius, β is v/c of incident particle, γ is $(1 - \beta^2)^{-1/2}$, A atomic weight of absorbing material, m_e the electron mass, N_A Avogadro's number, ρ the density of absorber, Z the atomic number of the absorbing material, I the mean excitation potential, z the charge of an incident particle in units of e , δ the density correction, C the shell correction and W_{max} the maximum energy transfer in one collision.

Different regions of the Bethe Bloch formula can be identified for different values of $\beta\gamma$, as shown in Fig. 1. For small values of $\beta\gamma < 0.1$ the incident particle loses most of its energy in ionization. At a value of $\beta\gamma \approx 3$ a minimum ionization is reached, the particle with $\beta\gamma \geq 3$ is called MIP. At large values of $\beta\gamma > 3$ the energy loss increases again due to the contribution of radiative processes.

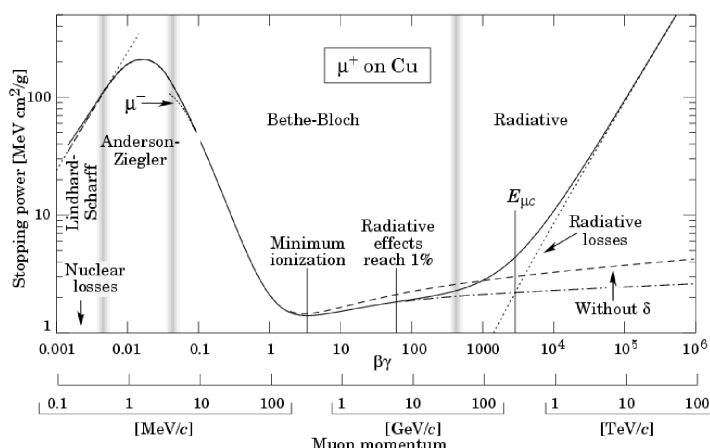


Figure 1: Stopping power for positive muons in copper, representing the average energy loss of muons penetrating copper normalized to copper density as a function of the muons kinetic energy [2].

MIPs travel across the detector's volume and lose just a percentage of its energy, which is statistically dispersed along the track. The total deposited energy is delimited by the thickness of the sensor. MIPs create a Landau signal in silicon with a most likely value (MPV) of about 80 e-h pairs per μm (Figure 2). The average energy necessary to create an electron-hole (e-h) pair in silicon is about 3.65 eV.

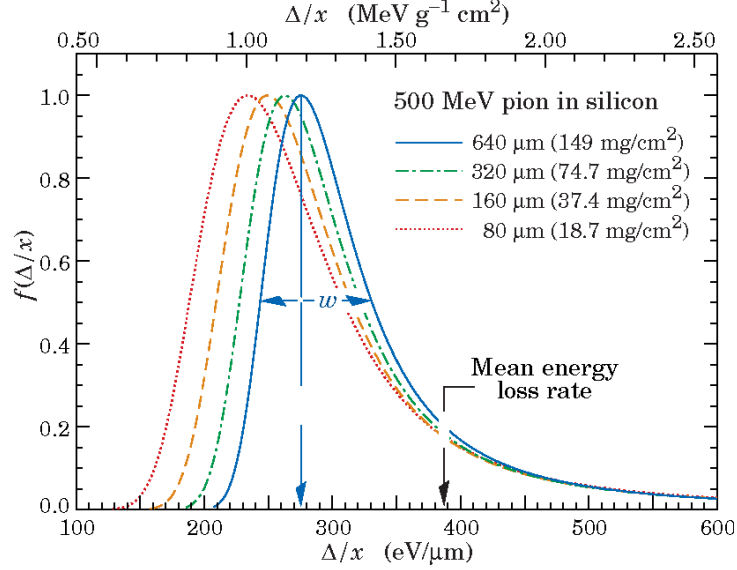


Figure 2: Energy-loss distribution for 500 MeV pions passing through a silicon layer: MIPs create a Landau signal in silicon with MPV of about 80 e-h pairs per μm . [2].

Detecting MIPs is quite challenging. Hence, they are crucial in the development and tuning of novel particle detectors.

1.2 Charge transport

Charge carriers produced by particles are separated by an electric field and collected on electrodes in silicon detectors. The charge carriers' movement causes a current across the electrical contacts, which the read-out electronics can detect. The charge transport can be distinguished by drift and diffusion.

When a charge is produced by a traversing particle, charge carriers in silicon move via drift in an electric field or via diffusion due to the concentration gradient. Because holes in silicon are less mobile than electrons, they are more prone to be trapped at impurities and defects.

Drift contributions are expected from charge carriers propagating in the depleted regions, while diffusion contributions are expected from charge carriers randomly propagating through the sensor's non-depleted parts [4]. When developing silicon detectors, we seek to maximize the depletion volume so that the particles move by drift. In this way, it is possible to control aspects such as charge sharing and the detector's time resolution.

1.3 Pixel detectors for lepton colliders

During the detection process in solid-state detectors, an incoming x-ray is absorbed by a photodiode and its energy is converted into electron-hole pairs through ionization. Under the influence of an electric field, electrons and holes then move in opposing directions. The signal produced by the moving charges is then measured and analyzed [3]. Hybrid detectors and monolithic detectors are the two most popular forms of pixel detectors.

In a hybrid detector, the photodiode and the readout electronics are connected by high-density interconnects called bump-bonds. This technique has the benefit of allowing absorption and signal processing to be adjusted independently. The drawback is that the pixel size is restricted to the interconnection process.

Monolithic detectors, as opposed to hybrid detectors, have both a photodiode for absorption and readout microelectronics for signal processing on a single chip. These detectors have distinct advantages, such as low noise and small pixels of less than $20\ \mu m$, which are not yet feasible with hybrid detector technology. Monolithic detectors will be the focus of this study.

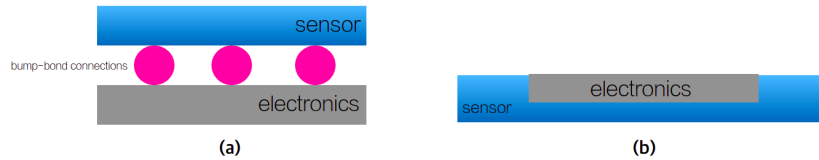


Figure 3: General schematics of: (a) hybrid detector, (b) monolithic detector

1.3.1 Monolithic detectors

For monolithic detectors, there are two pixel types: passive and active. Passive pixels only have a switching function that regulates the passage of signal charge to the sensor's periphery. The CCD sensor is the most successful with passive pixels. Active pixels, on the other hand, include transistors for active operations like amplification and processing. When active pixels are used in monolithic sensors, the device is referred to as a monolithic active-pixel sensor (MAPS).

Currently, two types of MAPS are being researched [2] (see Fig. 4): (a) detectors with big electrode designs (large fill factor, FF), in which the CMOS electronics is enclosed in the deep n-well, and (b) detectors with small electrode designs (small FF), in which the collecting electrode is separated (outside) from the protected electronics region.

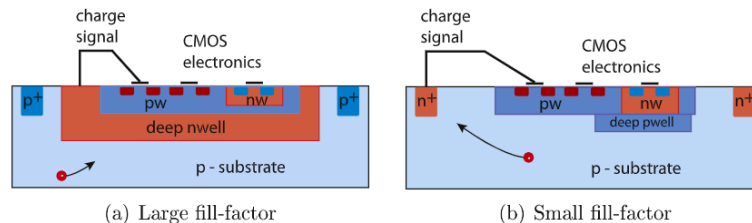


Figure 4: Two different CMOS geometries: (a) large fill-factor and (b) small fill-factor [7].

While the large FF design offers short average drift lengths and hence radiation hardness, it suffers from large input capacitance to the amplifier. The small FF technique provides all of the advantages associated with a small input capacitance but suffers from greater average drift lengths for the same pixel area. A process modification, which increases charge collection towards the small collection electrode by depleting the region beneath the electronics layer from two junctions, strengthens the lateral drift.

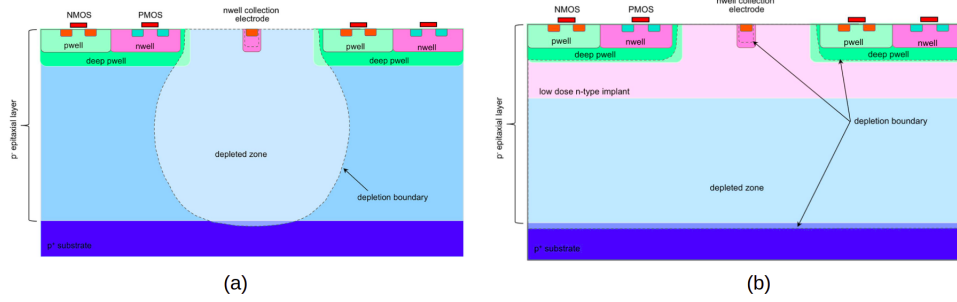


Figure 5: Schematic of a pixel in (a) the standard process and (b) the modified process [6]

In the standard process MAPS, depletion begins at the junction of the collection electrode and expands to the backside of the sensor with increasing reverse bias. However, it is difficult to laterally extend the depletion region into the epitaxial layer. A larger or even planar junction distinct from the collection electrode could be used to accomplish full depletion of the sensitive layer. [5]

1.4 EUDET Telescope

For R&D initiatives focusing on location-sensitive particle detection sensors, beam telescopes are essential instruments. A EUDET-type beam telescope family is used for test beams at the DESY synchrotron in Hamburg.

In DATURA Telescope, six Mimosas26 sensors are housed in an aluminum enclosure in the telescopes. A Mimosas26 (MAPS with fast binary readout) consists of 576×1152 pixels with $18.5 \mu\text{m}$ pitch. As a result, the active area measures $10.6 \times 21.2 \text{ mm}$. The chip measures $13.7 \text{ mm} \times 21.5 \text{ mm}$ in dimension.

Currently, the time resolution available on the telescope is not sufficient for many applications and track rates. And because the telescope has been in use for a long time, the modules should be updated to increase performance. The development of new sensors should improve the time resolution and maintain or increasing its spatial resolution to meet the requirements of the telescope for a lepton collider beam. Table 1 shows the silicon detector requirements at lepton colliders, compared to LHC (ATLAS/CMS). DESY is investigating 65 nm CMOS imaging technology to produce the next generation of pixel sensors as part of the Helmholtz Innovation Pool project Tangerine (Towards Next Generation Silicon Detectors).

Parameter	Lepton Collider	(HL-) LHC (ATLAS/CMS)
Material Budget	$<1\% X_0$ ($\sim 50 \mu m$ Si)	$10\% X_0$ ($\sim 50 \mu m$ Si)
Single-point resolution	$\leq 3 \mu m$	$\sim 15 \mu m$
Time resolution	$\sim 1 - 10$ ns	25 ns
Granularity	$\leq 25 \mu m \times 25 \mu m$	$50 \mu m \times 50 \mu m$
Radiation tolerance	$<10^{11} n_{eq}/cm^2$	$0(10^{16} n_{eq}/cm^2)$

Table 1: Performance of particle colliders



Figure 6: The DATURA telescope installed at the DESY testbeam area. The telescope mechanics and the sensor aluminum enclosure. [1]

2 TCAD Simulations of the Monolithic Sensors

Sensor development requires a high level of simulation. Synopsys' Technology Computer-Aided Design (TCAD) is a powerful simulation tool, widely used in the development of semiconductor devices. It provides tools for optimizing its performance.

The general strategy of the study is to vary some parameters within a range of values. The profile of the electric field is a result of the scan over the mentioned parameters. TCAD provides multiple classes of tools for different steps of the development and optimization of the semiconductor device [8]. For this work, the following tools were used:

- Sentaurus Workbench (SWB): It is the main tool interface. It supports the organization of simulation flow in a project.
- Sentaurus Structure Editor (SDE): This tool is used for process emulation. It is where the user defines the geometry and material doping concentrations of the sensor. Within SDE, the meshing operation must also be performed to define the accuracy and time of the simulation.
- Sentaurus Device (SDEVICE): In this tool, the user can simulate the electrical characteristics of devices created with SDE. It is possible to solve Poisson equations, transport

equations, and current continuity on the defined mesh for the given boundary conditions.

- Sentaurus Visual (SVISUAL) and/or Inspect: Tool to visualize the structures and results generated from the simulation.

The basic process flowchart of semiconductor device simulation is shown in Fig. 7.

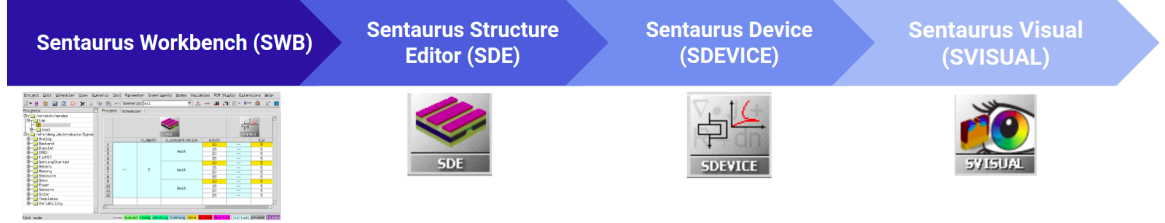


Figure 7: Simplified process flow of simulation tools by Synopsys Sentaurus TCAD 2020.

2.1 Model Details

Sentaurus Structure Editor (SDE) was used to model 65 μm monolithic CMOS with process modification to improve sensor depletion. The structure was proposed by Anastasiia Velyka and Adriana Simancas. Table 2 contains the layer structure of the designed device and the values used in simulation. The position of each layer is represented in Fig. 8.

Layer Description	Material	Doping Concentration [cm^{-3}]	Width [μm]	Depth [μm]	Extra Details
Electrodes	Al	–	1.5	1	Backside electrode occupies the entire device width, with same depth
Oxide	SiO_2	–	pitch dependant	0.2	–
Read-out (RO) Implants	Si	1E19	1	0.5	Phosphorus dopped
P-Well	Si	5E15	pitch dependant	0.5	Boron dopped
Deep P-Well	Si	5E15	pitch dependant	0.5	Boron dopped
P-type epitaxial layer	Si	2.657E13	pitch dependant	10	Boron dopped
Low dose n-type layer	Si	2E15	pitch dependant	3	Phosphorus dopped

Table 2: Design parameters of the monolithic device.

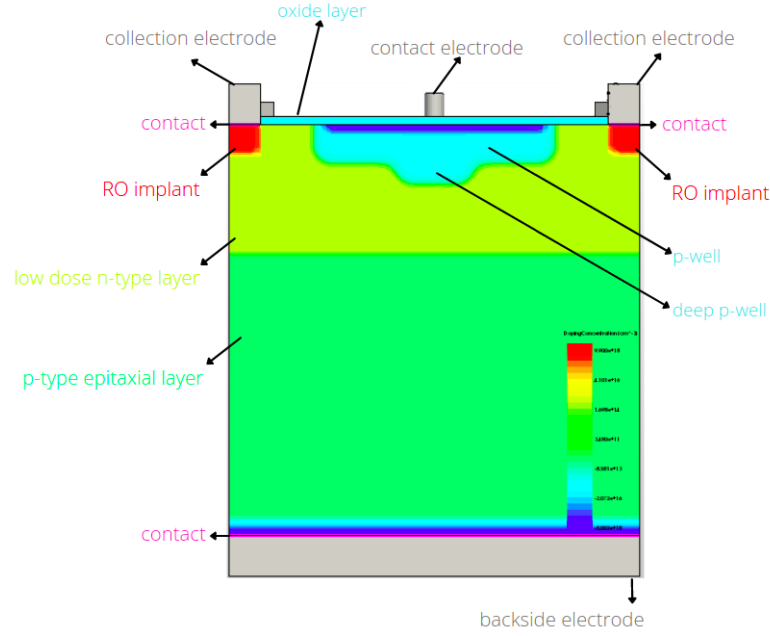


Figure 8: The position of the layers described in Table 8.

Simulations were carried out with various combinations of parameters, in order to study its influence in the depleted volume, the total electric field and lateral electric field. The parameters studied were the p-well and deep p-well opening, p-well bias voltage and backside electrode bias voltage, as shown in Fig. 9.

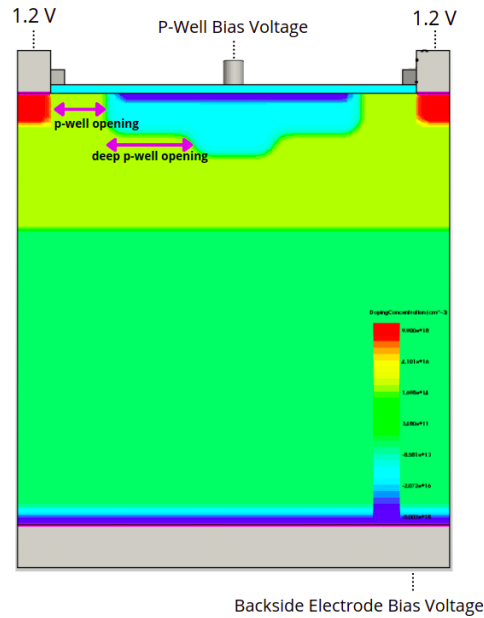


Figure 9: Parameters used in the simulations.

2.2 Simulation Workspace

In SWB, a workspace was created to run the model, set the specified parameters, ramp up the reverse bias voltage, and simulate the physical model. Fig. 10 shows how the workbench was configured.

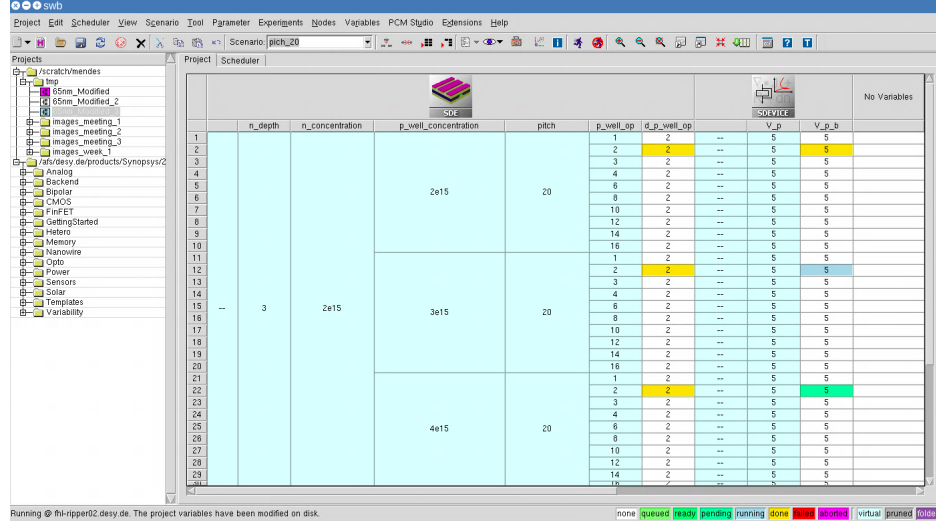


Figure 10: Sentaurus Workbench Project.

For each test, a parameter was selected to study and changed within a range of values while all the other parameters were fixed. Sentaurus Visual was then used to analyze the behavior of electric and lateral field and depleted volume

3 Simulation Results

After finishing building the device's 3D structure, electric field simulations are performed on the monolithic sensor. The parameters studied were the optimal operating voltage for the p-well and the backside and the distance between the p-well and the RO implants (p-well opening). The position of each parameter in the device geometry is shown in Figure 9.

3.1 Increasing p-well and backside voltage

The first simulation was performed by varying the p-well and backside bias values equally. Figure 9 shows the position of each bias contact. Table 3 shows the parameters used in the simulation.

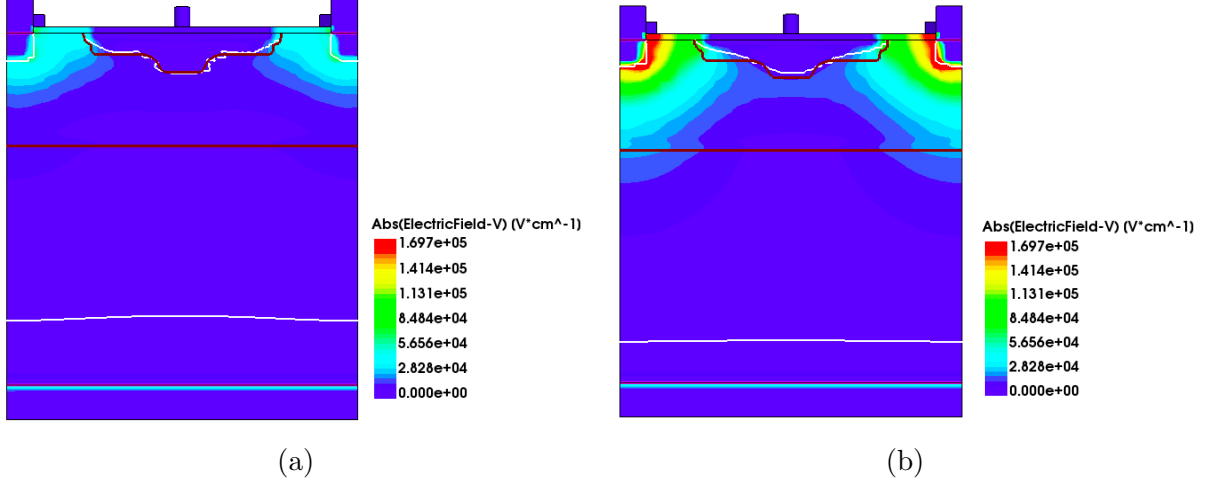


Figure 11: 2D cross section of a $10\ \mu\text{m}$ pitch sensor with: (a) -5V on the p-well and on the backside; (b) -20V on the p-well and on the backside.

Parameters	Value
Pixel pitch	$10\ \mu\text{m}$
P-well bias voltage	variable
Backside bias voltage	variable
P-well opening	$2\ \mu\text{m}$
Deep p-well opening	$2\ \mu\text{m}$

Table 3: Simulation parameters

Analyzing the 2D cross-section of the sensor, it was noted changes in the depletion region surrounding the p-well and at the bottom of the sensor (shown by the white lines in Figure 11). Figure 11.(b) shows that increasing the bias can create a high electric field inside the p-well. The electric field inside the p-well can negatively affect the electronics placed inside, removing its shielding protection.

Figure 12 shows the electric field distribution along a cutline in Z-axis, at a given X and Y position, for different backside and p-well voltages. The vertical lines represent the depletion region limits, passing through this cutline on the left side of the p-well. The results show an increase of the depletion volume in the bottom of the sensor layer.

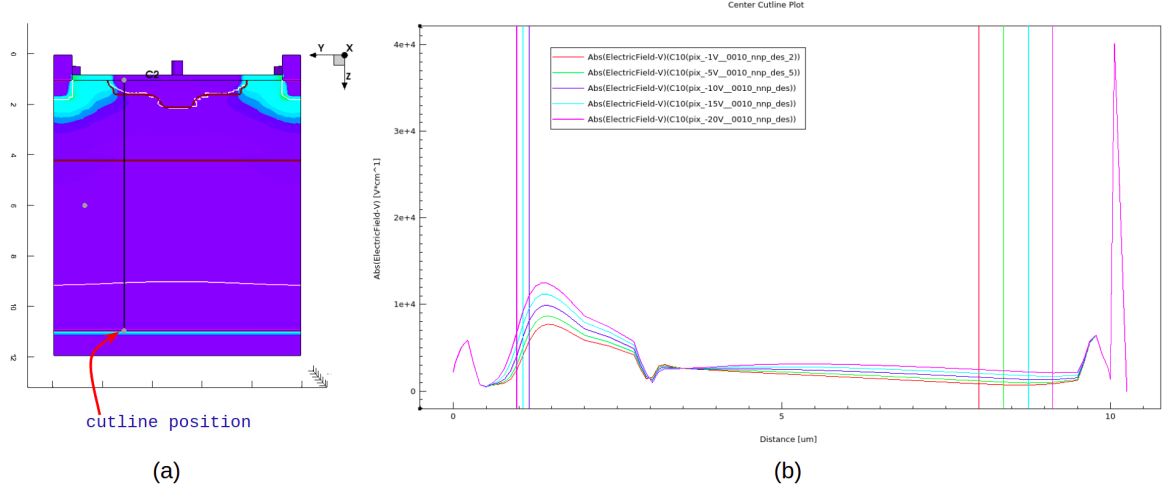


Figure 12: Electric field distribution for different voltage values at the p-well and backside. The vertical lines represent the depletion region limits, passing through the vertical cutline in the left side of the p-well as shown in the cross-section on the left (a).

3.2 Increasing backside voltage

To increase the depletion region without introducing depletion into the p-well, one possibility is to increase only the backside voltage. Therefore, simulations were executed fixing the p-well at -5 V and varying the backside voltage. Table 5 shows the parameters used in the simulation.

Parameters	Value
Pixel pitch	10 μm
P-well bias voltage	-5 V
Backside bias voltage	variable
P-well opening	2 μm
Deep p-well opening	2 μm

Table 4: Simulation parameters

Figure 13 shows the cross-sections of the sensor for multiple backside voltages. It is observed that the depletion line gets closer to the sensor backside, but it reaches breakdown at -11 V when a bump appears in the bottom depletion line.

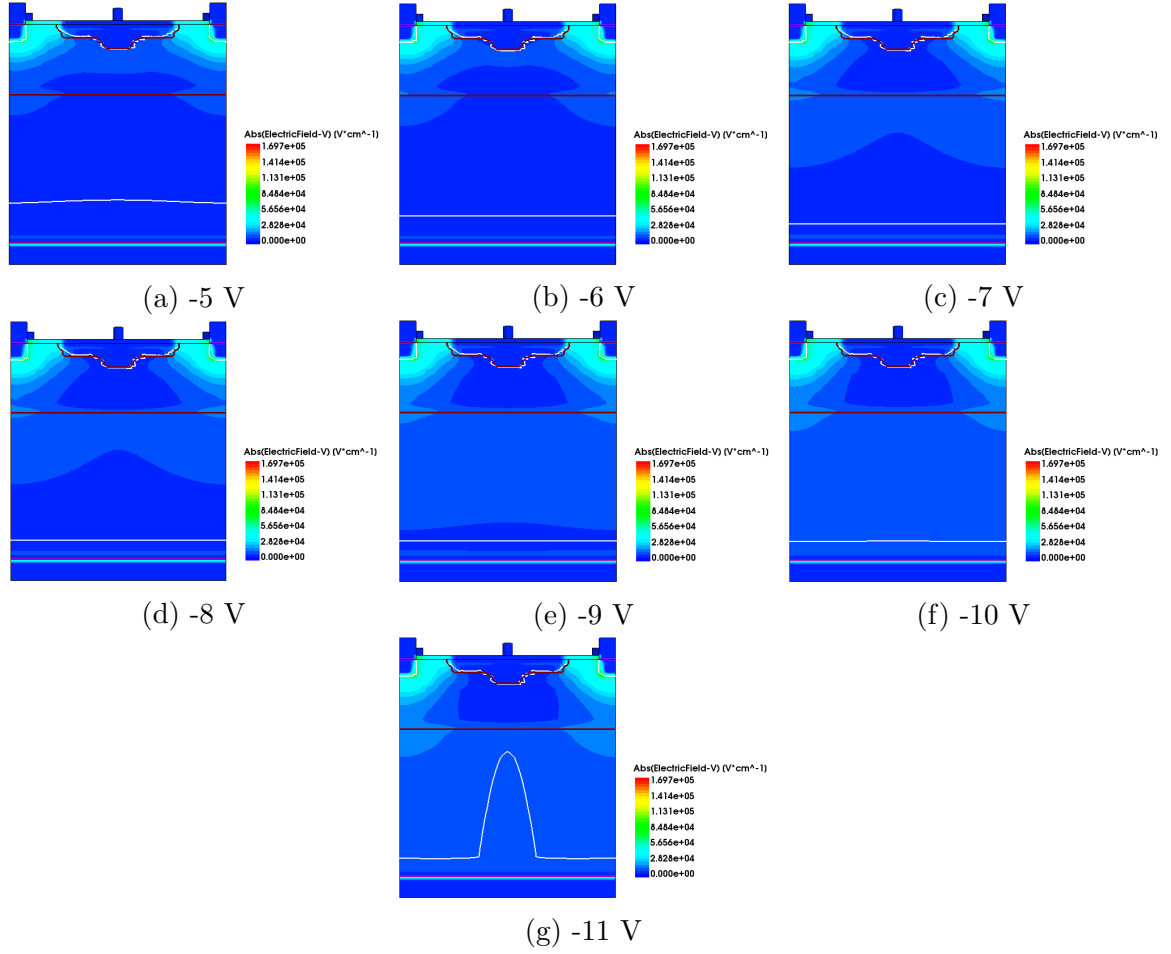


Figure 13: 2D cross section of a $10\ \mu\text{m}$ pitch sensor with p-well bias at -5 V, and backside voltages from -5 V to -11 V

The plot in Figure 14 shows the electric field distribution along a cutline in Z-axis, at a given X and Y position, for different backside voltages. The results verify that by increasing the backside, the depletion volume in the bottom of the sensor expands.

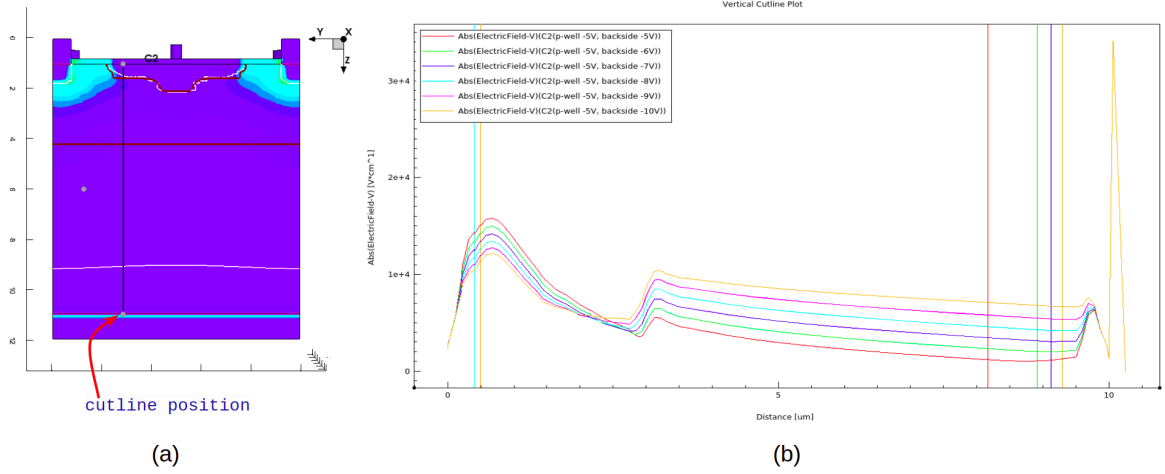


Figure 14: Electric field distribution for different voltage values with p-well and backside. The vertical lines represent the depletion region limits, passing through the vertical cutline in the left side of the p-well as shown in the cross-section on (a).

It is also observed that by increasing the backside voltage, the electric field in the sides of the sensor increases, slightly pushing the depletion line in the p-well (Figure 13.(a)), increasing the p-well size. In Figure 15.(a), the red circle indicates the area where the depletion line has increased in the p-well.

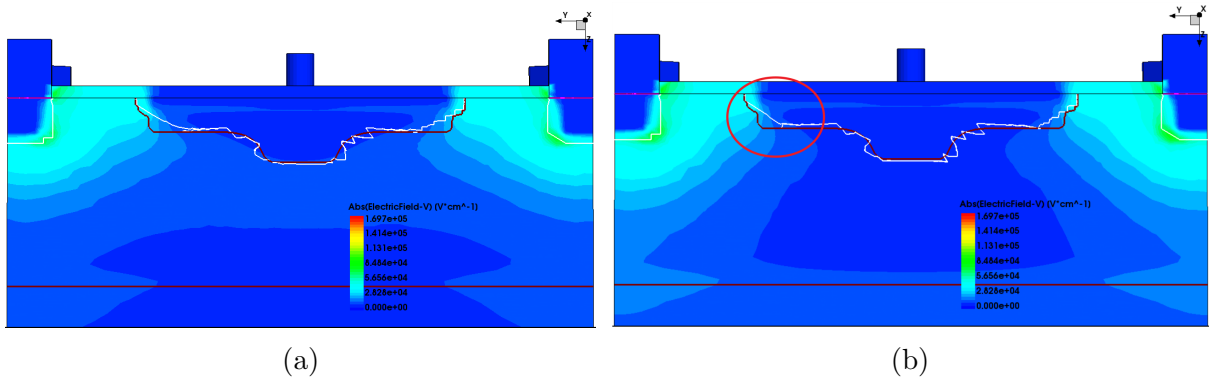


Figure 15: 2D cross section of a 10 μm pitch sensor with: (a) -5 V on the p-well and -5 V on the backside; (b) -5 V on the p-well and -9 V on the backside showing a small change in the depletion line (red circle).

3.3 Changing p-well opening

The parameters p-well opening and deep p-well opening are represented in Figure 9. In standard CMOS process, the electric field and the depletion volume are fundamentally different when the opening is changed. In modified process devices, simulations revealed that changing the opening values only influences the depleted line in the bottom of the sensor. Table 5 shows the parameters used in the simulation.

Parameters	Value
Pixel pitch	20 μm
P-well bias voltage	-5 V
Backside bias voltage	-5 V
P-well opening	variable
Deep p-well opening	2 μm

Table 5: Simulation parameters

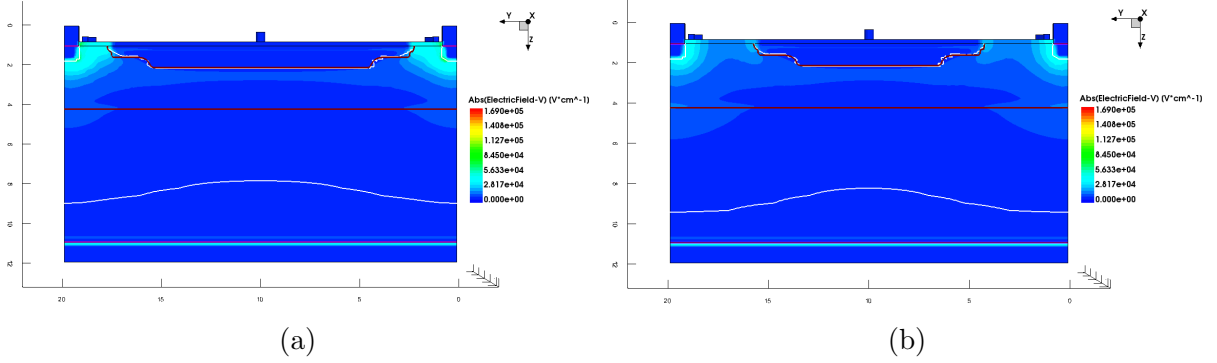


Figure 16: 2D cross section of a 20 μm pitch sensor with p-well and backside voltages at -5 V, and p-well opening of: (a) 2 μm and (b) 4 μm

The plot in Figure 17 shows the electric field distribution through a vertical cutline on the middle of the p-well as shown in the cross-section on Figure 14.(a). The results show a slight increase of the depletion in the bottom of the sensor.

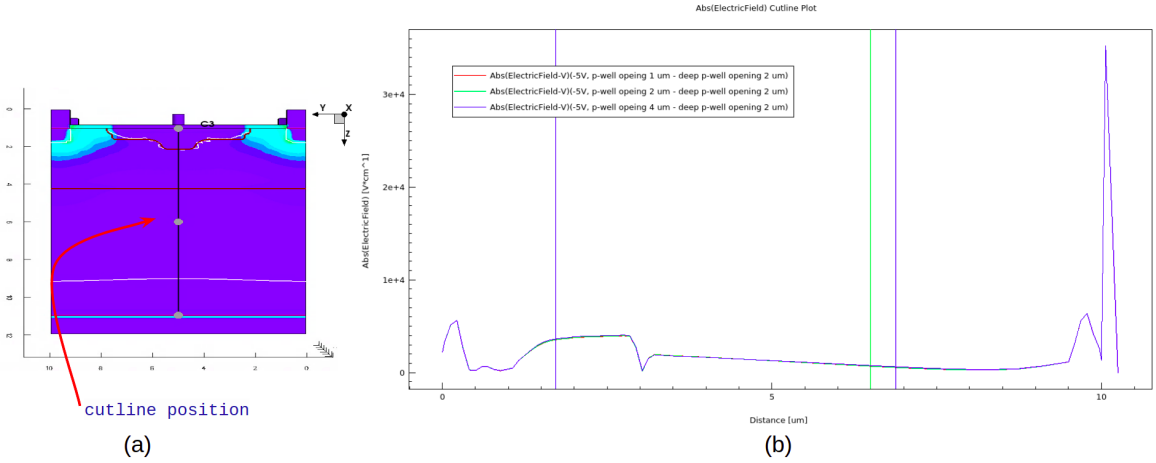


Figure 17: Electric field distribution (b) for p-well opening values of 1 μm , 2 μm , and 4 μm . The vertical lines represent the depletion region limits, passing through the vertical cutline in the middle the p-well as shown in the cross-section on the left (a).

Figure 18 shows the lateral electric field for p-well opening 2 μm and 4 μm . The increase in the lateral electric field in the corner regions allows faster charge collection by drift.

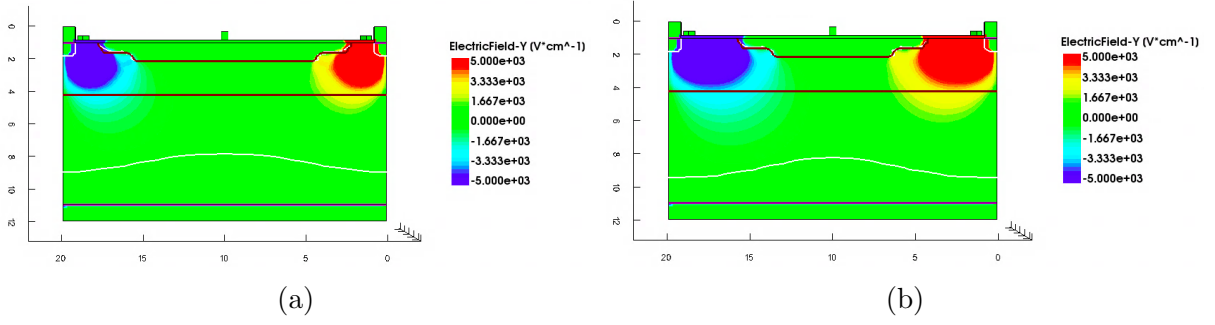


Figure 18: shows the lateral electric field for p-well opening (a) $2 \mu m$ and (b) $4 \mu m$

3.4 Conclusions

This report presents the advantages and constraints of changing the parameters of the sensor. In summary, from the simulations it was possible to conclude that:

- When the p-well bias voltage increases, it creates a high electric field inside the well.
The electric field inside the p-well can negatively affect the electronics placed inside, removing its shielding protection.
- The depletion region at the bottom of the sensor expands when the backside voltage increases.
- The electric field in the p-well corners grows as the backside voltage increases.
- A bigger p-well opening can increase depletion lines at the bottom of the sensor

Even though a larger p-well opening allows faster charge collection by drifting, the p-well size reduces as the p-well opening increases. Limiting the space for placing the CMOS electronics.

The goal of the manipulation of the parameters is to maximize the depleted volume and fast charge collection, as well as to have an efficient shielding of electronics inside the p-well. Further studies must employ the exact values of the sizes and doping concentrations provided by the manufacturers for greater optimization of the sensor efficiency.

References

- [1] Mimosa telescopes. <https://twiki.cern.ch/twiki/bin/view/MimosaTelescope/>. Accessed: 2021-08-23.
- [2] C Amsler, M Doser, M Antonelli, D Asner, K Babu, H Baer, H Band, R Barnett, E Bergren, J Beringer, et al. Passage of particles through matter. *Physics Letters B*, 667:267–280, 2008.
- [3] Takaki Hatsui and Heinz Graafsma. X-ray imaging detectors for synchrotron and XFEL sources. *IUCrJ*, 2(3):371–383, May 2015.
- [4] Magdalena Munker. Status of silicon detector R&D at CLIC. *PoS, VERTEX2018:033*, 2019.
- [5] W. Snoeys. Monolithic cmos sensors for high energy physics. *Nuclear Instruments and Methods in Physics Research Section A: Accelerators, Spectrometers, Detectors and Associated Equipment*, 924:51–58, 2019. 11th International Hiroshima Symposium on Development and Application of Semiconductor Tracking Detectors.
- [6] W. Snoeys, G. Aglieri Rinella, H. Hillemanns, T. Kugathasan, M. Mager, L. Musa, P. Riedler, F. Reidt, J. Van Hoorne, A. Fenigstein, and T. Leitner. A process modification for cmos monolithic active pixel sensors for enhanced depletion, timing performance and radiation tolerance. *Nuclear Instruments and Methods in Physics Research Section A: Accelerators, Spectrometers, Detectors and Associated Equipment*, 871:90–96, 2017.
- [7] N. Wermes. Pixel detectors ... where do we stand? *Nuclear Instruments and Methods in Physics Research Section A: Accelerators, Spectrometers, Detectors and Associated Equipment*, 924:44–50, 2019. 11th International Hiroshima Symposium on Development and Application of Semiconductor Tracking Detectors.
- [8] Yung-Chun Wu and Yi-Ruei Jhan. *Introduction of Synopsys Sentaurus TCAD Simulation*, pages 1–17. Springer Singapore, Singapore, 2018.